




Design and fabrication of drug-loaded alginate/hydroxyapatite/collagen composite scaffolds for repairing infected bone defects

Yongteng Song^{1,2}, Qingxi Hu^{1,2,3}, Qiong Liu^{4,5,6}, Suihong Liu^{1,2,7}, Yahao Wang^{1,2}, and Haiguang Zhang^{1,2,3,*} 

¹ Rapid Manufacturing Engineering Center, School of Mechatronic Engineering and Automation, Shanghai University, Shanghai 200444, China

² Shanghai Key Laboratory of Intelligent Manufacturing and Robotics, Shanghai University, Shanghai 200072, China

³ National Demonstration Center for Experimental Engineering Training Education, Shanghai University, Shanghai 200444, China

⁴ Translational Research Institute of Brain and Brain-Like Intelligence, Shanghai Fourth People's Hospital, School of Medicine, Tongji University, Shanghai 200434, China

⁵ Clinical Research Center for Anesthesiology and Perioperative Medicine, Tongji University, Shanghai 200434, China

⁶ State Key Laboratory of Molecular Engineering of Polymers, Fudan University, Shanghai 200438, China

⁷ Centre for Translational Bone, Joint and Soft Tissue Research, Faculty of Medicine, University Hospital Carl Gustav Carus, Technische Universität Dresden, 01307 Dresden, Germany

Received: 23 June 2022

Accepted: 30 November 2022

Published online:

1 January 2023

© The Author(s), under exclusive licence to Springer Science+Business Media, LLC, part of Springer Nature 2022

ABSTRACT

In bone tissue engineering, repairing infected bone defects is an enduring challenge. The development of bone tissue engineering scaffolds with a local antimicrobial drug delivery system is a promising method to overcome this challenge. Thus, in this work, a sodium alginate (SA)/hydroxyapatite (HAP)/collagen (COL) multimaterial composite scaffold carrying amoxicillin (AMX) porous hydroxyapatite microspheres (mHAPs) (AMX@mHAPs) was fabricated utilizing a three-dimensional (3D) printing and freeze-drying composite process for infected bone defects. The morphology of the scaffolds was evaluated by SEM, which indicated that the prepared scaffold contained microporous structures and embedded drug-loaded microspheres into hydrogels with a diameter of $18.62 \pm 2.77 \mu\text{m}$. The drug-loaded availability of the scaffold was investigated via FTIR, which showed that AMX could be loaded successfully on mHAPs by a stirring process and hydrogen-bonding forces. Thereafter, evaluation of the physicochemical properties of the fabricated scaffold revealed that the mechanical properties of the scaffold could be enhanced by the addition of AMX@mHAPs (increased appr. 1.71-fold compared to the AMX@mHAPs-free scaffold at 15% strain), and the swelling property could also be altered. Furthermore, in vitro drug release and antibacterial tests suggested

Handling Editor: Yaroslava Yingling.

Address correspondence to E-mail: haiguang_zhang@i.shu.edu.cn

<https://doi.org/10.1007/s10853-022-08053-3>

that the fabricated scaffold had excellent drug release and long-term antibacterial properties. Finally, the cytocompatibility of the composite scaffolds was assessed by seeding rabbit adipose-derived stem cells (rASCs), and the results proved that cells could attach, proliferate and migrate on the scaffold and exhibited favorable cytocompatibility. Together, these results demonstrated that the preparation process of the composite scaffold is feasible and that the fabricated SA/HAP/COL composite scaffold loaded with AMX@mHAPs has great potential for infected bone defect repair.

Introduction

Bone is the framework of the human body, playing a supporting and protective role [1]. Factors such as trauma, infection, osteoporosis, and tumor resection easily cause large bone defects, which seriously affect the normal life of patients [2]. It is common knowledge that the human body cannot fully heal large-scale bone defects, and external surgical intervention is necessary to repair normal bone defects by graft implantation [3]. To date, the traditional treatment methods for bone defect repair include autogenous bone transplantation, allogeneic bone transplantation, artificial bone transplantation, and artificial bone replacement [4, 5]. However, these approaches have some problems, such as insufficient bone supply, immune rejection, secondary injury, and poor biocompatibility. Especially for the repair of infected bone defects with higher requirements for transplantation, traditional methods are more difficult to fulfill [6, 7]. Fortunately, the emergence of tissue engineering may make up for the deficiency of traditional methods in repairing bone defects.

Therefore, using a bone tissue engineering approach that combines engineering and life sciences, a biocompatible antibiotic-loaded bone tissue engineering scaffold has been prepared and exhibits great potential in bone defects, especially in infected bone defects [8, 9]. The traditional preparation methods of bone tissue engineering scaffolds include chemical/gas foaming, solvent casting, particle/salt immersion, etc. [10]. However, traditional approaches have some disadvantages, such as individual shape-controllable manufacturing, pore diameter, porosity, and poor pore connectivity [11].

To overcome the above challenges, three-dimensional (3D) printing as an additive manufacturing (AM) process has become an ideal approach to

prepare bone scaffolds [12]. In particular, extrusion-based 3D printing is more advantageous due to its wide range of materials and the characteristics of carrying cells and drugs, which have been widely used in bone tissue engineering [13] to fabricate transplantable bone scaffolds with high porosity and pore connectivity, controllable shape and size, and drug loading [14, 15]. Furthermore, this technology can also achieve personalized bone tissue repair and regeneration. However, although 3D-printed bone scaffolds have outstanding development prospects, some limitations remain; such as suitable biomaterial ink and delivery of drugs, particularly for infected bone tissue defects.

Due to the advantages of avoiding stress concentration, degradability, and drug loading, biodegradable drug-loaded scaffolds have been widely investigated in the field of bone tissue engineering [16]. As a 3D polymer matrix, hydrogels are similar to the extracellular matrix of human soft tissues in physical properties [17], have been widely used to prepare biodegradable scaffolds due to their high permeability and porosity, perfect biocompatibility, and can be used as carriers for cell growth and sustained drug release [18, 19]. Furthermore, the superior printability also makes hydrogels an ideal material for biological 3D printing [20].

Various natural biomaterials with excellent biocompatibility have been used to manufacture hydrogel bone scaffolds, such as collagen (COL) [21], sodium alginate (SA) [22], hydroxyapatite (HAP) [13], chitosan (CS) [23], and gelatin (GEL) [24–26]. However, due to the limited mechanical properties, printability, and drug-loaded properties of hydrogels prepared from a single biomaterial, their further clinical application is limited [27, 28]. Hence, studies have shown that the mechanical properties, printability, and biocompatibility of bone scaffolds can be significantly improved by compounding different

biomaterials [23, 29], such as the combination of SA and GEL as a biomaterial ink, which exhibits excellent printability and self-standing properties for the fabrication of volumetric scaffolds [24]. However, pure hydrogel materials cannot promote the regeneration of bone tissue very well. Thus, the combination of COL with osteoinductive properties [30] and hydrogel materials (such as SA) could boost the growth of bone tissue while ensuring the printability of scaffolds. In addition, as the main inorganic component of human bone tissue, HAP exhibits high biological activity and osteogenic capacity, as well as excellent physical and chemical [31, 32]. Meanwhile, as the main organic protein component of human bone, COL can also induce mineral deposition and enhance the mineralization process [30], the combination of HAP and COL can improve the mechanical properties of COL and provide favorable bone conductivity [21]. In addition, SA has been widely used in regenerative medicine and tissue engineering because of its non-toxicity, biodegradability, and excellent biocompatibility [22]. Hence, we speculate that the bone scaffold prepared by compounding SA, COL, and HAP is more conducive to bone tissue regeneration and bone defect repair. It is worth mentioning that the infection of bone tissue can also be prevented and treated by loading antimicrobial drugs on composite biomaterial scaffolds [33].

Previous research suggested that for infected bone defects, local antibiotic treatment has been proven to promote the bioavailability of drugs and reduce the adverse effects of frequent use of drugs [34, 35]. In the current research, the antibiotics commonly used in infected bone defects are vancomycin [36], doxorubicin [37], nanosilver [38], amoxicillin (AMX) [39], and so forth. AMX, as a broad-spectrum antibiotic, can be used to treat a variety of bacterial infections and can easily spread to body fluids and tissues [40]. It is worth mentioning that after the scaffold is implanted in the human body, the sustained release of drugs is very significant for the treatment of infected bone defects [41]. In recent decades, some nanoscale drug delivery systems have provided new ideas for more effective drug delivery (such as drug sustained release) in the field of tissue engineering [42]. In bone tissue engineering, porous hydroxyapatite microspheres (mHAPs), as drug carriers for AMX, are widely used due to their perfect drug adsorption, biocompatibility, bone conductivity, and favorable drug-loaded and release properties [43–45].

Hence, adding AMX porous mHAPs (AMX@mHAPs) as a local drug delivery system to the bone scaffold may give the scaffold remarkable drug release and antibacterial capability.

Keeping the above mind, in this work, the author developed a drug-loaded SA/HAP/COL composite bone scaffold (AMX@mHAPs-SHC) by combining freeze-drying and extrusion 3D printing techniques for infected bone defects. The physicochemical and biological properties of the fabricated scaffolds were systematically evaluated; they exhibited favorable mechanical properties, outstanding drug release properties, and great potential for infected bone defect repair.

Materials and methods

Materials

Sodium alginate (SA, 9005-38-3, 20201110), collagen (COL, from cowhide, 98%, YR765514-500 g), and amoxicillin (AMX, 26787-78-0, A129660-5 g) were purchased from Aladdin Reagent Co., Ltd. (Shanghai, China). Hydroxyapatite nanoparticles (HAP, 1306-06-5, 40 nm, acicular) were obtained from Shanghai Hualan Chemical Technology Co., Ltd. (Shanghai, China). Genipin (GP, 6902-77-8, 98%) was provided by Linchuan Zhixin Biotechnology Co., Ltd. (Jiangxi, China). Glucosactone (GDL, 90-80-2, 99%, D810428-100 g) was acquired from Shanghai Macklin Biochemical Co., Ltd. (Shanghai, China). Porous hydroxyapatite microspheres (mHAPs, type I, 20 μ m, yy20a0010-10 g) were purchased from Henan Huier Nano Technology Co., Ltd. (Henan, China).

Preparation of AMX@mHAPs

To obtain mHAPs loaded with AMX (AMX@mHAPs), stirring, centrifugation and freeze-drying were used in this investigation. Specifically, 0.3 g mHAPs were dispersed in a certain amount of deionized water by an ultrasonic instrument (frequency is 40 kHz, dispersion time is 5 min), and 800 r/min was stirred at constant speed at room temperature to obtain the mHAPs pellet. Afterwards, 90 mL of AMX solution with different concentrations (0.5, 1, and 2 mg/mL) was added into to suspended pellet within 20 min. After dripping, the suspension was stirred for 24 h and centrifuged, and the

supernatant was discarded and washed three times using deionized water. Subsequently, the slurry was frozen at $-80\text{ }^{\circ}\text{C}$ for 6 h. Then, the frozen slurry was put into a freeze-drying machine (temperature is $-80\text{ }^{\circ}\text{C}$, vacuum degree is 8 Pa) for 24 h, and AMX@mHAPs powder was obtained and stored at $4\text{ }^{\circ}\text{C}$ for further use.

Preparation of AMX@mHAPs-SHC

Figure 1 shows schematic diagrams of the preparation process of the SA/HAP/COL composite drug-loaded hydrogel bone scaffold containing AMX@mHAPs (AMX@mHAPs-SHC). The preparation process of the pre-crosslinked hydrogel used to print AMX@mHAPs-SHC is as follows:

First, 0.6 g of HAP nanoparticles, 0.1 g of GP, and 0.3 g of COL were added to 30 mL of deionized water and then stirred at $37\text{ }^{\circ}\text{C}$ for 50 min to form a uniform slurry. Afterwards, 1.2 g SA was put into the above slurry and stirred for 30 min to obtain the SA/HAP/COL hydrogel with a COL-GP crosslinked network. Next, as the previously reported [46], 0.3 g GDL and 0.3 g AMX@mHAPs were added to the above hydrogel and stirred for 1 h to acquire the pre-crosslinked SA/HAP/COL hydrogel with the SA- Ca^{2+} and COL-GP double-crosslinked network.

Furthermore, AMX@mHAPs-SHC was formed based on the composite process of freeze-drying and 3D bioprinting. In particular, the pre-crosslinked

hydrogel was printed through the PTC-RD331 triaxial dispensing control system (experimental parameters: needle diameter 0.84 mm; extrusion pressure: 1.25 MPa; printing speed: 15 mm/s; extrusion temperature: $26\text{ }^{\circ}\text{C}$) to obtain the designed composite drug-loaded scaffold with a size of $20 \times 20 \times 5\text{ mm}^3$. Subsequently, the scaffolds were further cross-linked in 10 wt% CaCl_2 solution for 1 h, washed with deionized water 3 times, and soaked for 12 h. After that, the scaffolds were placed at $-80\text{ }^{\circ}\text{C}$ for 6 h. Finally, they were freeze-dried in a vacuum dryer (temperature: $-80\text{ }^{\circ}\text{C}$; vacuum: 8.0 Pa) for 8 h and removed for further use. At this point, the scaffold was prepared. Figure 2 shows the internal structure of AMX@mHAPs-SHC. AMX@mHAPs-SHC is mainly composed of the SA- Ca^{2+} crosslinked network, COL-GP crosslinked network, and AMX@mHAPs.

Micromorphology characterization of the scaffold

The freeze-dried scaffolds were sprayed with gold by sputtering to characterize their microstructures, and the microstructures of the unloaded AMX@mHAPs scaffold (SHC) and AMX@mHAPs-SHC were characterized by tungsten filament scanning electron microscopy (SEM; Hitachi SU-1500, Hitachi, Japan). The diameter of 60 drug-loaded microspheres in

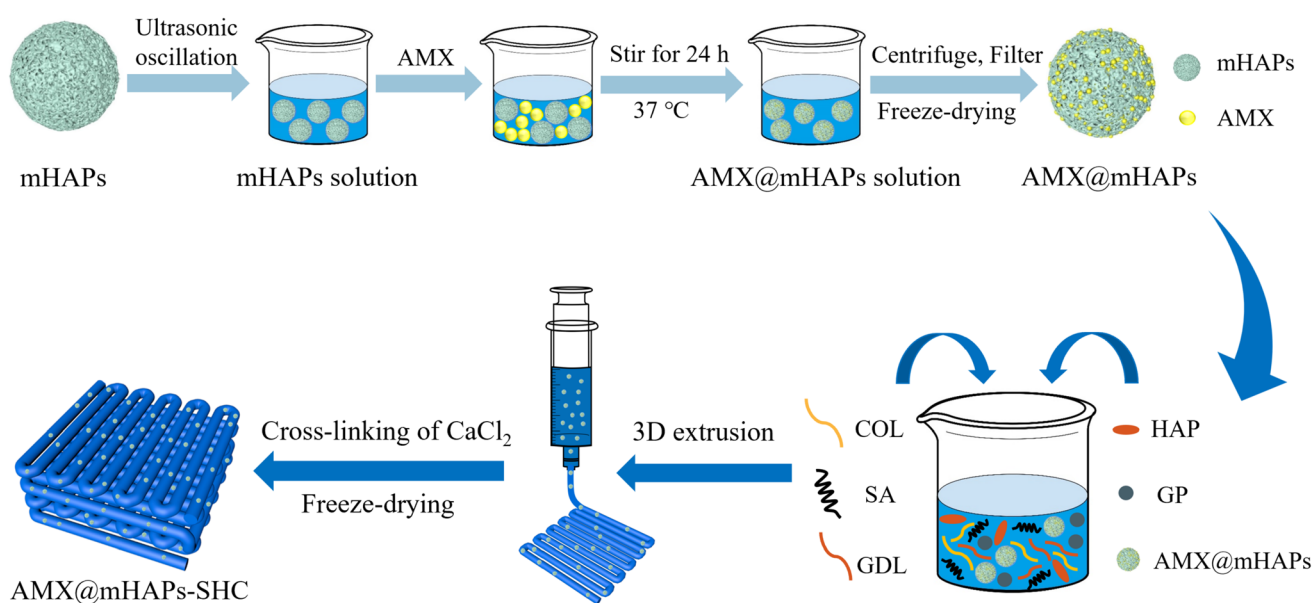


Figure 1 Schematic diagram of the preparation process of AMX@mHAPs-SHC.

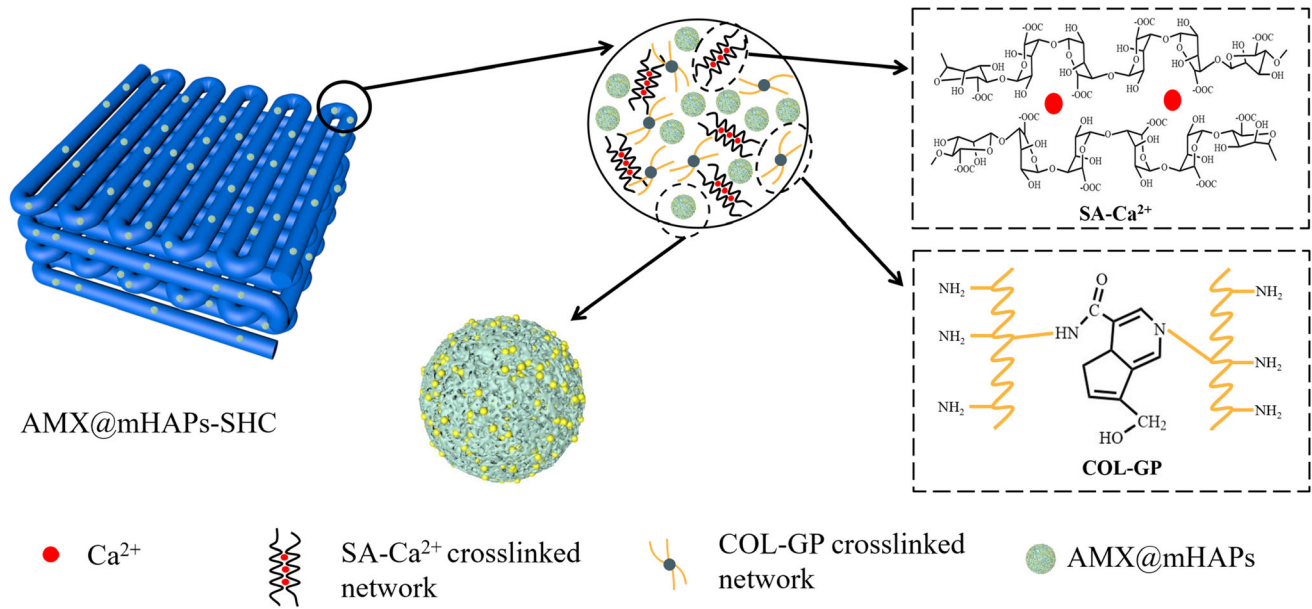


Figure 2 Schematic diagram of the internal structure of AMX@mHAPs-SHC.

AMX@mHAPs-SHC SEM images was measured and analyzed by Nano Measurer 1.2 software.

Fourier transform infrared spectroscopy analysis

To analyze the chemical composition and functional group composition of each sample, the chemical composition and functional groups of AMX, mHAPs, AMX@mHAPs, SHC, and AMX@mHAPs-SHC were analyzed by Fourier transform infrared spectrometry (FTIR; AVATAR370, Nicolet, USA). The FTIR spectra of 4000 ~ 400 cm⁻¹ were recorded, and the resolution was 1 cm⁻¹.

Mechanical properties test

The compression properties of the freeze-dried scaffolds were tested by freeze-drying using a WDW-1 materials testing machine (ZWICK BIAxIAL-10KN, Germany) according to a previous protocol [23]. The stress–strain curves of SHC and AMX@mHAPs-SHC were obtained, and the compression modulus of each scaffold was calculated from the slope of the stress–strain curve. The testing scaffold samples were mounted and compressed in the vertical direction at a strain rate of 2 mm/min at RT. Six samples in each group were tested.

Swelling analysis

The swelling characteristics of SHC and AMX@mHAPs-SHC were evaluated by mass change over time. Briefly, the initial dry weight (M_{S0} g) of different scaffolds was measured, and then the scaffolds were immersed in phosphate buffer solution (PBS, pH = 7.4) at room temperature for 1, 2, 3, 4, 6, 8, 10, 12, 14, 16, 18, 20, 22, 24, 26, and 28 h. Next, the excess moisture on the surface of the scaffolds was absorbed with filter paper, and the wet weight (M_{S1} g) of the scaffold was weighed and compared with the M_{S0} g of the corresponding scaffold. The swelling rate (S) was calculated from the following equation:

$$S = [(M_{S1} - M_{S0}) / M_{S0}] \times 100\%$$

The SHC was used as the control group. Each swelling test was carried out on three samples, and the average value was taken.

In vitro drug release

In this examination, the drug release property of AMX in vitro was evaluated by PBS immersion and drug absorbance tests. Primarily, each printed AMX@mHAPs-SHC of 50 mg was immersed in 50 mL PBS solution in a centrifuge tube, and then the centrifuge tubes were incubated at 37 °C. The 2 mL release medium was removed at the designated time points (4, 8, 12, 24, 36, 48, 60, 72, 96, 120, 144, 192, 240,

and 288 h), and the same volume of fresh PBS solution was supplemented. The absorbance of AMX in the medium released at each time interval was detected by ultraviolet spectrophotometer (UV-1800, MAPADA, China) at 272 nm, and the drug release curve of AMX was obtained by comparing the absorbance-concentration standard curve of AMX (The corresponding absorbance of amoxicillin was measured at the concentration of 0, 0.148, 0.222, 0.296, 0.370, 0.444, and 0.519 mg/ml, respectively, and the absorbance-concentration standard curve was formed by linear fitting). In this study, the data of each sample were determined more than three times, and the average value was acquired. Furthermore, the AMX@mHAPs used in this experiment were prepared at different concentrations of AMX (0.5, 1, and 2 mg/mL; referred as below: 0.5-AMX, 1-AMX, and 2-AMX, respectively).

Evaluation of antibacterial properties

The antibacterial activity of each scaffold (SHC, 0.5-AMX, 1-AMX, and 2-AMX) was assessed by observing the bacteriostatic zone of *Escherichia coli*, and SHC was used as the control group. *Escherichia coli* (E. coli; GIM1.442, GDMCC, China; the concentration of bacteria is approximately 10^8 CFU/mL) suspended in tryptone soybean broth (TSB) was spread on agar plates. Afterwards, the printed scaffold samples with a diameter of 6 mm and thickness of 1 mm were placed on agar plates and incubated at 37 °C for 24, 72, and 120 h. Eventually, the growth and proliferation of bacteria and the diameter of the bacteriostatic zone were observed.

Cell characterization

Cell adhesion

To sterilize the fabricated scaffolds, SHC (control group) and AMX@mHAPs-SHC (experimental group) were immersed in 75% alcohol for 1 h, washed 3 times with PBS solution, and then soaked in *Petri* dishes with fresh culture medium (RPMI1640) for 4 h. Subsequently, rabbit adipose-derived stem cells (rASCs; Procell Life Science & Technology Co., Ltd. China) were seeded into each scaffold at a density of 5.0×10^5 cells/mL, and the cell-seeded scaffolds were cultured in a CO₂ incubator (5%) at 37 °C for 4 h to allow cells to adhere to the scaffolds. After

that, fresh culture medium was added until the scaffolds were immersed. After 1, 3, and 5 days of incubation, the cell-seeded scaffolds were stained for 20 min by a live/dead cell staining kit (Biovision, Inc., San Francisco, CA). In this research, the staining solution was prepared by mixing 0.75 μL of Live-Dye and 1.5 μL of PI in 1 mL of staining buffer. The cells on the scaffold were observed under an inverted fluorescence microscope (LH-M100CB-1, Nikon, Japan).

Cell proliferation

The cell proliferation of fabricated scaffolds was evaluated by using the indirect CCK-8 method according to a previous approach [26]. The SHC (control group) and AMX@mHAPs-SHC (experimental group) were sterilized by immersing in 75% alcohol for 1 h and rinsed with PBS three times to remove residual alcohol from the scaffolds. Subsequently, the scaffold samples were soaked in 10 mL of the culture medium for 48 h. Then, rASCs were seeded into a 96-well plate at a concentration of 5×10^4 cells/well, and 100 μL of soaking extract of each scaffold sample and culture medium (positive control group) were added and cultured in a 5% CO₂ cell incubator at 37 °C. After the cells were cultured for 1, 3, and 5 days, 10 μL of Cell Counting Kit-8 reagent (CCK-8; Key-GEN Biotech CO., Ltd., China) was added to each microwell and incubated with CCK-8 at 37 °C for 3 h. The absorbance was determined at a wavelength of 450 nm by using a microplate reader (Infinite 200 Pro, Tecan Group Ltd., Switzerland).

Statistical analysis data

All data are presented as the mean ± standard deviation (SD) and were analyzed using Origin 2021 statistical software. One-way analysis of variance (one-way ANOVA) was used to analyze the difference between groups, and $P \leq 0.05$ was considered statistically significant.

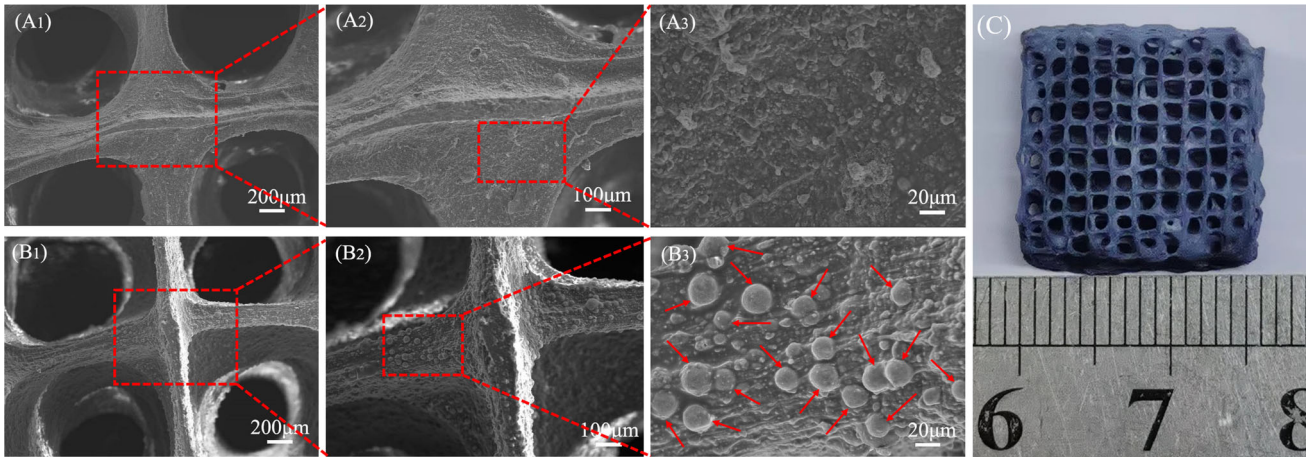


Figure 3 SEM images of the fabricated SHC and AMX@mHAPs-SHC: (A₁, A₂, and A₃) SHC; (B₁, B₂, and B₃) AMX@mHAPs-SHC; (C) Macrograph of the 3D-printed AMX@mHAPs-SHC.

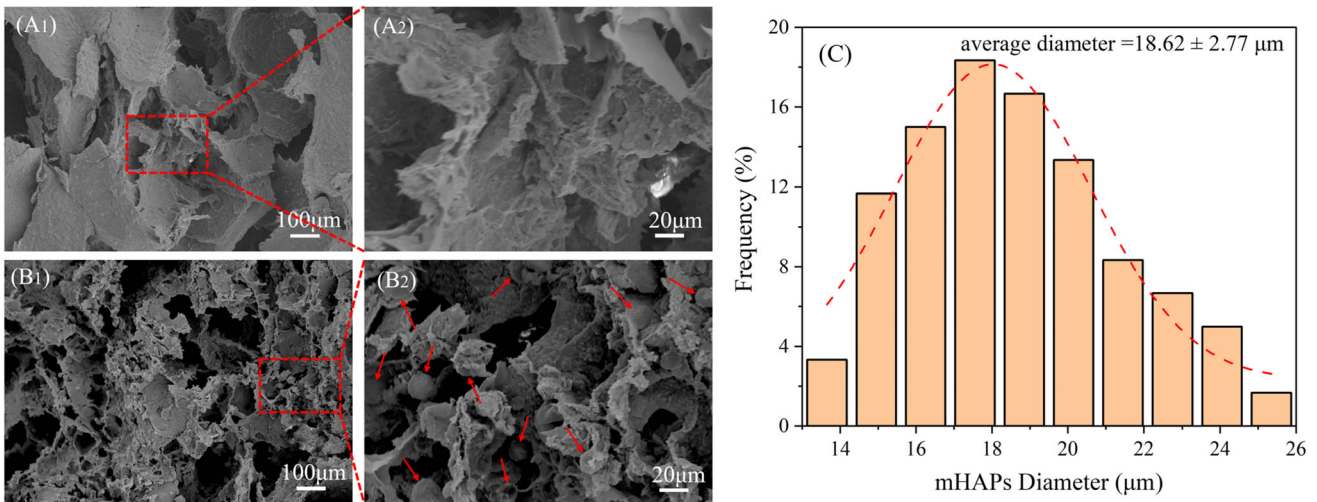


Figure 4 SEM cross-sectional view of SHC and AMX@mHAPs-SHC and particle size analysis diagram of AMX@mHAPs: (A₁ and A₂) SHC; (B₁ and B₂) AMX@mHAPs-SHC; (C) particle size analysis results of AMX@mHAPs in Figure B₁.

Results

Micromorphology characterization of the scaffold

Figures 3 and 4 show the SEM images of SHC and AMX@mHAPs-SHC (the drug-loaded microspheres are marked with a red arrow in the figure). The surface SEM characterization results of each sample are shown in Fig. 3. In contrast to SHC, some drug-loaded microspheres were also attached to the surface of AMX@mHAPs-SHC, and the existence of drug-loaded microspheres enhanced the surface roughness of the composite drug-loaded scaffolds, which were conducive to cell adhesion and spreading

[47]. As shown in Fig. 4, compared with SHC, there was a host of drug-loaded microspheres with an average diameter of $18.62 \pm 2.77 \mu\text{m}$ in AMX@mHAPs-SHC, which were attached to the micropore wall of the scaffold or embedded in the scaffold. Moreover, the introduction of drug-loaded microspheres made the scaffold have a highly interconnected 3D porous structure of approximately 100 μm in size, which was favorable for improving the biological activity and drug release properties of the scaffolds [48, 49].

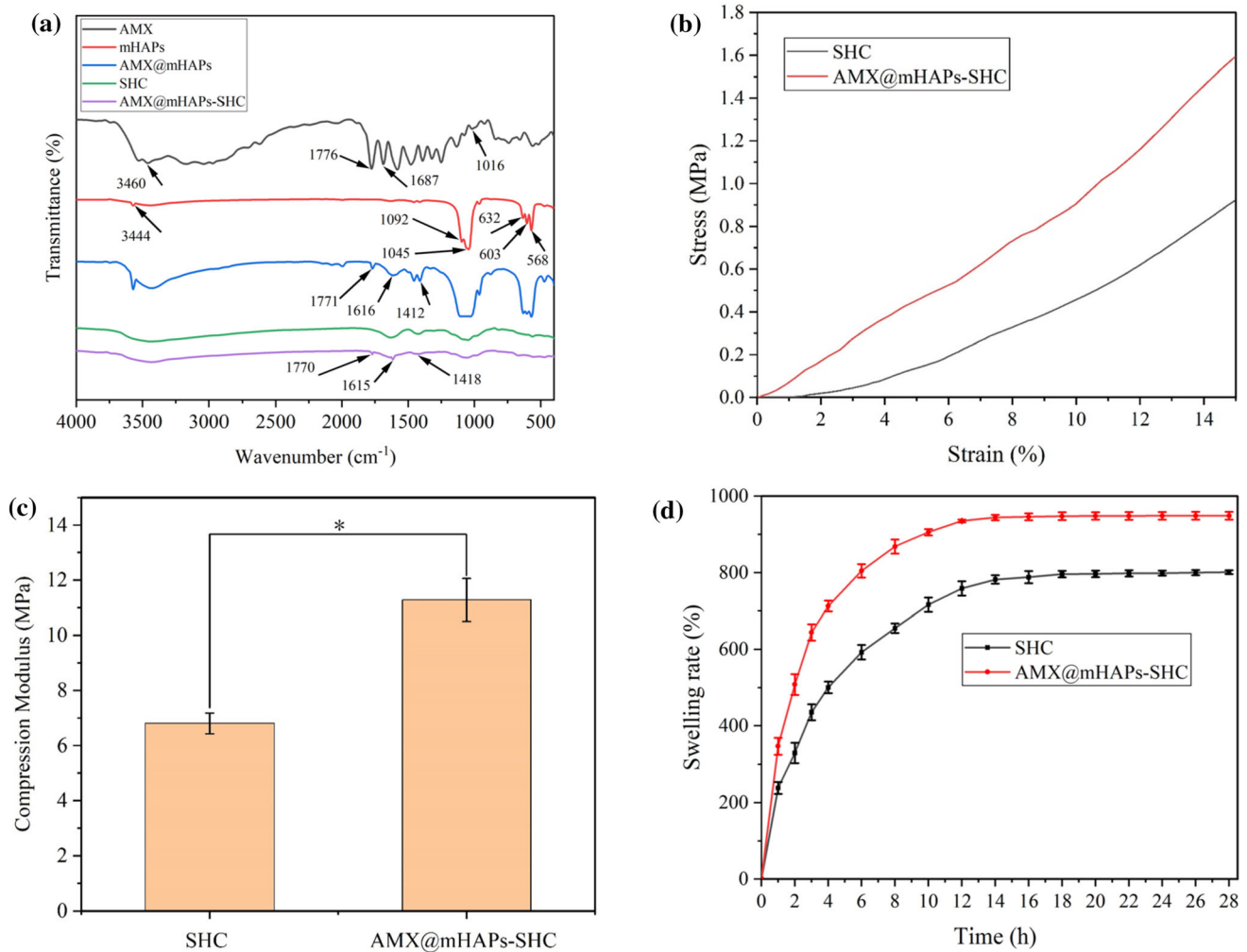


Figure 5 **a** FTIR spectra of AMX, mHAPs, AMX@mHAPs, SHC, and AMX@mHAPs-SHC. **b** Compressive stress–strain curves of SHC and AMX@mHAPs-SHC. **c** The compressive modulus of SHC and AMX@mHAPs-SHC. **d** Swelling rate

curves of SHC and AMX@mHAPs-SHC after soaking in PBS solution. The error bars represent the standard deviation (B, C: $n = 6$; D: $n = 3$), and a value of $*p \leq 0.05$ was considered statistically significant.

Fourier transform infrared spectroscopy analysis

Figure 5a shows the FTIR spectra of each sample. PO_4^{3-} characteristic bands of the mHAPs sample were found in the peaks at 1092, 1045, 603, and 568 cm^{-1} , and the $-\text{OH}$ bands at 3444 and 632 cm^{-1} were characteristic of a typical hydroxyapatite FTIR spectrum, indicating that the composition of the mHAPs sample is hydroxyapatite. For the AMX sample, the typical characteristic bands at 3460 and 1776 cm^{-1} were attributed to the $\text{O}-\text{H}$ and $\text{N}-\text{H}$ stretching, and $\text{C}=\text{O}$ stretching of β -lactamic in the AMX structure; other peaks at 1687 and 1016 cm^{-1} were assigned to $\text{C}=\text{O}$ stretching of amide and $\text{C}-\text{O}$

bending vibration in AMX, respectively [50, 51]. The above FTIR results revealed that the AMX sample is amoxicillin. Besides, three characteristic bands were observed at 1771, 1616, and 1412 cm^{-1} in the spectra of the AMX@mHAPs sample, which were attributed to $\text{C}=\text{O}$ stretching of the β -lactamic ring, aromatic $\text{C}=\text{C}$ bending, and symmetric COO^- stretching, which also proved the physical mixing of AMX and mHAPs [52]. Furthermore, compared with SHC, the absorption bands of AMX@mHAPs-SHC at 1770, 1615, and 1418 cm^{-1} proved that AMX@mHAPs were successfully combined with the composite scaffold.

Mechanical properties test

To evaluate the influence of loading AMX@mHAPs on the mechanical properties of the scaffolds, the compression mechanical performance of SHC and AMX@mHAPs-SHC was tested to investigate their compression properties. The stress–strain curves and compressive modulus experimental results of each scaffold are presented in Fig. 5b and c. The results showed that under 15% strain, the average compressive stress of AMX@mHAPs-SHC was 1.62 ± 0.09 MPa, which was 1.71 times that of SHC (0.95 ± 0.06 MPa), and the average compressive modulus was 11.28 ± 0.78 MPa, which was 65.9% higher than that of SHC (6.80 ± 0.38 MPa). Thus, the compression property of the composite scaffold could be boosted by adding AMX@mHAPs.

Swelling analysis

The curves of the swelling ratio of SHC and AMX@mHAPs-SHC over time are shown in Fig. 5d. Obviously, the swelling ratio of each scaffold changed rapidly in the first 4 h and approached swelling equilibrium after 14 h. The swelling ratios of SHC and AMX@mHAPs-SHC at swelling equilibrium were $948.50 \pm 10.20\%$ and $800.84 \pm 4.98\%$, respectively. The results suggested that the addition of

AMX@mHAPs could appropriately increase the swelling ratio of composite scaffolds.

In vitro drug release

In this work, the in vitro drug release properties of AMX from AMX@mHAPs-SHC were investigated by ultraviolet spectrophotometry. As seen from the drug release curves of each scaffold (0.5-AMX, 1-AMX, and 2-AMX) demonstrated in Fig. 6a, in the process of drug release, all scaffolds demonstrated similar drug release performance, including early fast release and subsequent sustained release. Specifically, a majority of the drugs were released quickly in the first 96 h and then decreased to the complete release rate at 288 h, showing a long-term drug release effect. At 288 h, the corresponding drug release concentrations of 0.5 mL AMX, 1 mL AMX, and 2-AMX reached 0.1430 ± 0.0081 , 0.1998 ± 0.0072 , and 0.2592 ± 0.0054 mg/mL, individually.

Moreover, from the release curve of AMX, it was determined that the release rate and total release amount of AMX gradually increased with the increase in AMX concentration. In conclusion, the scaffold has distinguished drug release properties.

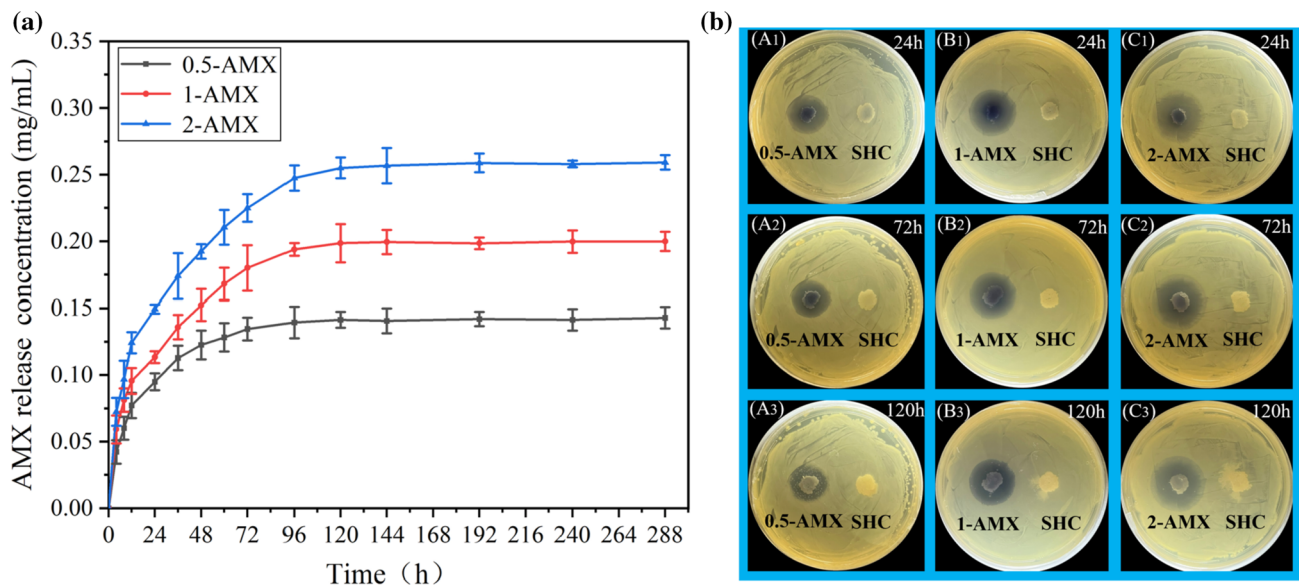


Figure 6 a Drug release curves of AMX@mHAPs-SHC in vitro. b Antibacterial effect of each scaffold on *E. coli* after different culture times. SHC and 2-AMX: (A₁) 24 h; (A₂) 72 h; (A₃) 120 h;

SHC, 0.5-AMX, 1-AMX, and 2-AMX: (B₁) 24 h; (B₂) 72 h; (B₃) 120 h. The error bars represent the standard deviation ($n = 3$).

Evaluation of antibacterial properties

The antibacterial properties of each scaffold (SHC, 0.5-AMX, 1-AMX, and 2-AMX) were estimated by the inhibition zone method. In this study, SHC was used as the control group. The experimental results are shown in Fig. 6b. Apparently, no inhibition zone was found in SHC without AMX@mHAPs loading, suggesting that the scaffold had no antibacterial activity against *E. coli*. Nevertheless, AMX@mHAPs-SHC produced a significant inhibition zone, which indicated that the scaffold could effectively inhibit the growth of *E. coli*. Furthermore, by observing the diameter of the bacteriostatic zone of each scaffold, it could be noticed that with the increase in AMX concentration, the diameter of the bacteriostatic zone of *E. coli* gradually increased, and the bacteriostatic effect was better. After 120 h of culture, no significant reduction in the inhibition zone of AMX@mHAPs-SHC was observed. The above results indicated that AMX@mHAPs-SHC had long-term and significant antibacterial activity against *E. coli*, and the antibacterial properties of AMX@mHAPs could be regulated by changing the concentration of AMX.

Cell characterization

Cell adhesion

The biocompatibility of scaffolds is one of the essential factors for further biomedical applications. To examine the biocompatibility of each scaffold, ADSCs were inoculated on SHC and AMX@mHAPs-SHC for 1, 3, and 5 days, and the morphology of ADSCs on the scaffold was observed by an inverted fluorescence microscope. Figure 7a displays live/dead fluorescence images of cells on each group of scaffolds after 1, 3, and 5 days of culture. After staining the cells on the scaffolds, the living cells were green, and the dead cells were red. The image revealed that the cells were long spindle-shaped in SHC and AMX@mHAPs-SHC, and dead cells were rarely found. These results indicate that each scaffold showed favorable cell adhesion and high cell viability. Furthermore, compared with the first day, with the extension of culture time, the number of cells on the scaffold extended significantly on the third and fifth days. Overall, AMX@mHAPs-SHC exhibited excellent biocompatibility, which was favorable for cell adhesion, spreading, and proliferation.

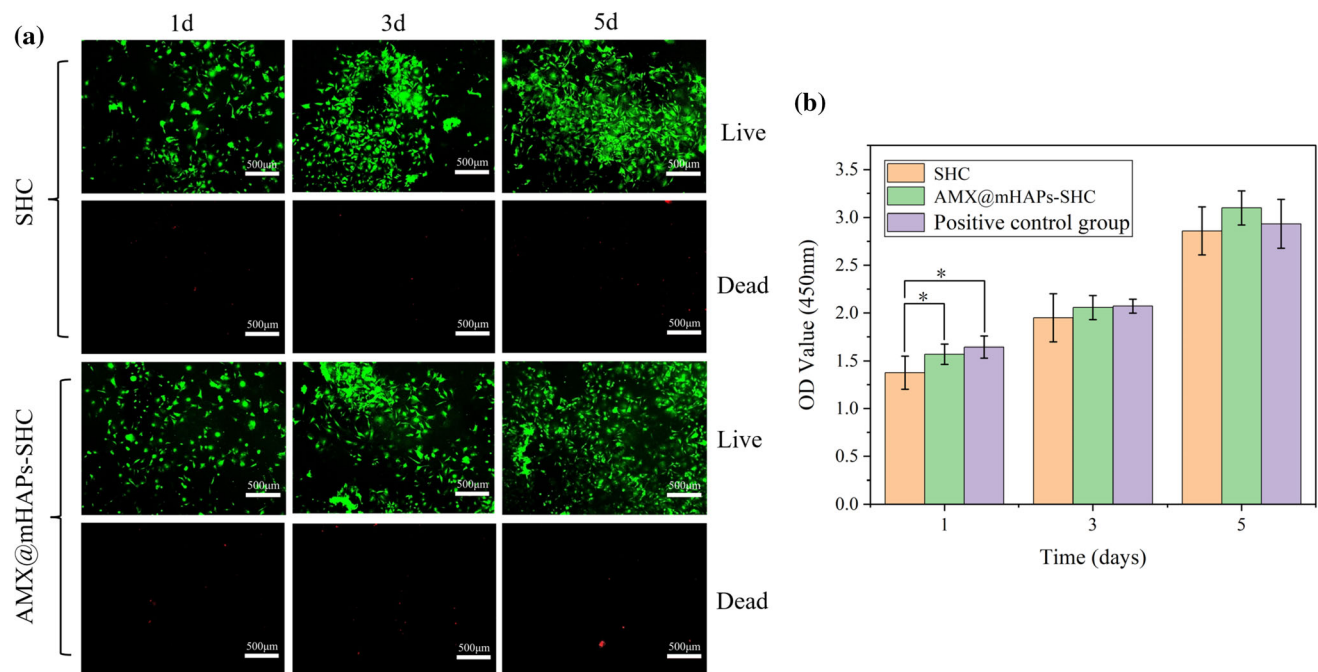


Figure 7 a Live/dead cell fluorescence images of ADSCs on SHC and AMX@mHAPs-SHC after culturing for 1, 3, and 5 days. b The CCK-8 assay data analysis of ADSCs after culturing for 1,

3, and 5 days. The error bars represent the standard deviation ($n = 3$), and a value of $*p \leq 0.05$ was considered statistically significant.

Cell proliferation

To further research the cell biocompatibility and proliferation of scaffolds, the effects of soaking extracts of different scaffolds on the proliferation of ADSCs were assessed by CCK-8 assay. Figure 7b displays the CCK-8 test results for the control group (SHC), the experimental group (AMX@mHAPs-SHC), and the positive control group (culture medium). After 1, 3, and 5 days of culture, the OD value of each group increased gradually and maintained the same trend of cell proliferation. Significant error analysis suggested that there was no significant difference between the third day and the fifth day, except for the significant difference in OD values among the three groups on the first day. Specifically, the OD value of the experimental group was slightly higher than that of the control group from 1 to 5 days. The OD value of the experimental group was close to but slightly lower than that of the positive control group after 1 and 3 days of culture. Nevertheless, the OD value of the experimental group was higher than that of the positive control group after culturing for 5 days, probably because the existence of the antibiotic AMX promotes cell growth [44]. The above results illustrated that AMX@mHAPs were nontoxic to the scaffolds, and the introduction of AMX@mHAPs into the scaffolds had no adverse effect on cell proliferation. In short, AMX@mHAPs-SHC has favorable cytocompatibility and can make cells grow and proliferate well.

Discussion

In biomedical engineering, excellent repair of tissue engineering bone defects demands a three-dimensional biocompatible scaffold, which can ensure cell attachment and proliferation and provide sufficient mechanical support for bone tissue healing [53]. In recent years, although the area of bone tissue engineering has developed rapidly, the repair of infected bone defects is still a challenging goal [54]. The purpose of this work was to develop an AMX@mHAPs-SHC with an AMX@mHAPs drug delivery system, which has favorable bacteriostatic properties, sustained drug release properties, and biocompatibility. The scaffold can continuously deliver antibiotics to the bone defect during bone healing and better realizes the repair of the infected bone defects.

Natural bone is a composite material composed of inorganic and organic components [55]. Organic SA is a natural biocompatible polymer, which is widely used in various biomedical fields. It has high biocompatibility and is easy to gel, and can form stable gel by adding divalent cations, such as Ca^{2+} , into SA aqueous solution at room temperature [14, 56]. HAP is the main inorganic component of bone, which has many similarities with natural bone in chemistry and structure, remarkable biocompatibility, and bone conductivity, and has been proven to promote bone tissue regeneration [21, 43]. The combination of HAP and SA can significantly improve the mechanical properties of scaffolds while simulating the natural bone composition [29]. In this investigation, the mixing of GDL can reduce the pH value of the gelation system, allowing Ca^{2+} to be gradually released from HAP nanoparticles and cross-linked with SA [57], thus increasing the viscosity of the pre-crosslinked hydrogel and facilitating printing and forming [58]. Therefore, the introduction of GDL can indirectly improve the printability of gel system. Moreover, combined with the further cross-linking of the pre-crosslinked hydrogel by CaCl_2 solution, the SA- Ca^{2+} crosslinked network was formed to enhance the mechanical properties of the scaffold. COL has favorable biocompatibility and osteogenic induction performance, and mixing it with HAP can improve cell adhesion, proliferation, and activity [30]. Besides, the surface of COL contains sites that promote osteoblast adsorption and mineral deposition, so the addition of COL is beneficial to the perfect combination of scaffolds with surrounding bone tissues [59]. However, poor mechanical strength limits its further application. GP is a natural crosslinking agent extracted from gardenia fruit that has low cytotoxicity. Studies have shown that the lysine, hydroxylysine, and arginine amino acid residues within COL could react with GP, so that GP can cross-linked with COL perfectly [60]. Thus, in this research, GP was used as the crosslinking agent of COL to form a COL-GP crosslinked network, which was combined with the SA- Ca^{2+} crosslinked network to make up the double-crosslinked network (Fig. 2) [46].

Bone scaffolds with a certain mechanical strength can provide sufficient mechanical support for the growth of new bone tissue [61]. Mechanical performance tests showed that the average compressive stress of AMX@mHAPs-SHC (1.62 ± 0.09 MPa) was

1.71 times of SHC under 15% strain (Fig. 5b), and the compression modulus of AMX@mHAPs-SHC (11.28 ± 0.78 MPa) was 1.66 times of SHC (Fig. 5c). Meanwhile, its compressive stress was within the normal range of human cancellous bone (0.2–80 MPa) [62], and compression modulus also meet the requirements of human natural cancellous bone (0.01–0.2 GPa) [12]. Thus, after mixing with the drug-loaded microspheres, the mechanical properties of the composite scaffolds were greatly promoted. The main cause is probably that AMX@mHAPs can be used as the reinforcement phase of the scaffold and the stress points of its internal structure, thus promoting the transfer of stress from the scaffold matrix material to AMX@mHAPs [46]. Furthermore, it is believed that scaffold materials with a certain swelling rate are beneficial to the exchange of cell nutrients and metabolites [63]. The scaffold with outstanding swelling behaviors maintains a greatly hydrated state similar to the ECM as well as promotes cell proliferation [64]. In this investigation, the swelling rate of each scaffold changes rapidly in the first 4 h, showing strong water absorption. After that, the swelling rate increased slowly until the swelling equilibrium was reached after 14 h. The swelling rate of AMX@mHAPs-SHC ($948.50 \pm 10.20\%$) was somewhat improved compared with that of SHC ($800.84 \pm 4.98\%$) (Fig. 5d) when the dissolution equilibrium was reached. Furthermore, by comparing the volume and size of each scaffold before and after swelling, it was shown that the swelling of the scaffold had no significant effect on the characteristic resolution of the printing scaffold. Hence, AMX@mHAPs-SHC have high swelling properties and hydrophilicity than SHC. The main reason may be the introduction of AMX@mHAPs, which made the gelation network have a highly interconnected porous structure inside the composite drug-loading scaffold (Fig. 3B1), thus improving the water absorption capacity of the scaffold. Notably, AMX@mHAPs itself also has a certain water absorption capacity. In summary, the loading of AMX@mHAPs improved the physical and chemical properties of the composite drug-loaded scaffolds to some extent.

For the prevention and treatment of infected bone defects, the AMX@mHAPs local antimicrobial drug delivery system was introduced in this work. As the drug carrier, mHAPs have massive nano micropores on their surface, which have a larger specific surface

area and better drug delivery capability than needle-like HAP [45]. Successful drug loading is crucial to the drug loading system. The FTIR spectra in Fig. 5a demonstrated that AMX was more strongly adsorbed by mHAPs. The combination principle of AMX and mHAPs is that mHAPs establish a chemical bond with the polar groups (-NH, -OH) of AMX through the action of hydrogen bonding [65]. The drug release test suggested that all scaffolds showed similar drug release performance, including rapid release in the early stage and continuous release in the later stage, and we can adjust the drug release rate and total drug release of AMX in the scaffold by adjusting the load concentration of AMX. Specifically, most of the AMX was released quickly within the first 96 h, and the release rate decreased to a uniform release in the following time until 288 h (Fig. 6a), indicating that the scaffold had a certain drug sustained release effect. The reason is probably that a mass of AMX was adsorbed on the internal micropores and surface of mHAPs. When the AMX on the surface of the microspheres was released at a rapid rate, there would be a concentration difference of AMX between the interior and the surface of the microspheres, which made the AMX in the drug-loaded microspheres gradually spread to the surface through the micropore, thus realizing the slow release of the drug. The antibacterial experiment of *E. coli* illustrated that AMX@mHAPs-SHC had outstanding long-term antibacterial activity (Fig. 6b). Hence, the early fast release of antibiotics can make the scaffold maintain a high concentration of AMX at the initial stage, thus obtaining rapid anti-infective properties and providing a sterile environment for early bone regeneration [31]. In the following period, the drug was released slowly until it was completely released. In summary, the existence of AMX@mHAPs endowed the drug-loaded scaffolds with excellent drug release performance and long-term antibacterial properties.

To accomplish the complete repair of the infected bone tissue, the prepared bone scaffolds should have both excellent physicochemical properties and biocompatibility. The ADSCs culture experiment in vitro demonstrated that AMX@mHAPs-SHC had distinguished biocompatibility, and the addition of AMX@mHAPs had no adverse effect on cytocompatibility. Therefore, we proposed an efficient method to prepare AMX@mHAPs-SHC, which can be used for the local sustained release of antibacterial

drugs and the repair of infected bone defects. In this study, the physicochemical and biological properties of composite drug-loaded scaffolds were examined, and some effective experimental data and results were obtained. Nevertheless, the deficiency is that the performance of composite drug-loaded scaffolds with different AMX@mHAPs contents has not been deeply investigated. To solve this problem, the influence of drug-loaded microspheres content on the performance of bone scaffolds will be further evaluated in the future.

Conclusion

In this work, based on freeze-drying and extrusion 3D printing techniques, a multimaterial composite drug-laden AMX@mHAPs-SHC bone tissue scaffold was successfully fabricated for infected bone defects. To efficiently achieve the loading and release of AMX antimicrobials, AMX@mHAPs were prepared by stirring, centrifugation, and freeze-drying, and it was demonstrated that AMX was successfully adsorbed by mHAPs. The results of compression performance indicated that the average compression modulus of AMX@mHAPs-SHC (11.28 ± 0.78 MPa) is 1.66 times that of SHC (6.80 ± 0.38 MPa), and its compression performance was greatly improved. Furthermore, the swelling property of AMX@mHAPs-SHC could be adjusted by adding AMX@mHAPs, and the hydrophilicity of the composite scaffold could be increased. The fabricated composite scaffold exhibited excellent drug loading efficiency and release performance and could maintain long-term drug release and antibacterial activity, which provided a remarkable aseptic environment for the repair of bone defects. In addition, rASCs could survive, attach, and proliferate on the fabricated scaffold, indicating the nontoxicity and cytocompatibility of the preparation process and fabricated scaffold. Together, all the results demonstrated that this composite preparation method and fabricated composite drug-laden AMX@mHAPs-SHC scaffold have great potential for the clinical application of infected bone defect repair.

Acknowledgements

The authors acknowledge funding support from the National Natural Science Foundation of China (Grant Nos: 52175474).

Declaration

Conflict of interest The authors declared that they have no conflicts of interest. This article does not contain any studies with human or animal subjects performed by any of the authors.

References

- [1] Deng ZW et al (2020) A novel 3D printed bioactive scaffolds with enhanced osteogenic inspired by ancient Chinese medicine HYSA for bone repair. *Exp Cell Res* **394**. <https://doi.org/10.1016/j.yexcr.2020.112139>.
- [2] Wang H et al (2020) A novel vehicle-like drug delivery 3D printing scaffold and its applications for a rat femoral bone repairing in vitro and in vivo. *Int J Biol Sci* **16**:1821–1832. <https://doi.org/10.7150/ijbs.37552>
- [3] Sun H et al (2020) 3D printing of calcium phosphate scaffolds with controlled release of antibacterial functions for jaw bone repair. *Mater Design* **189**:108540. <https://doi.org/10.1016/j.matdes.2020.108540>
- [4] Li JL et al (2021) Immobilization of bioactive vascular endothelial growth factor onto Ca-deficient hydroxyapatite-coated Mg by covalent bonding using polydopamine. *J Orthop Transl* **30**:82–92. <https://doi.org/10.1016/j.jot.2021.06.002>
- [5] Cao YX et al (2019) 3D printed beta-TCP scaffold with sphingosine 1-phosphate coating promotes osteogenesis and inhibits inflammation. *Biochem Biophys Res Commun* **512**:889–895. <https://doi.org/10.1016/j.bbrc.2019.03.132>
- [6] Li K et al (2021) A novel biocomposite scaffold with antibacterial potential and the ability to promote bone repair. *J Biomater Appl* **36**:474–480. <https://doi.org/10.1177/0885328221994448>
- [7] Wang Q et al (2015) 3D-printed atsttrin-incorporated alginate/hydroxyapatite scaffold promotes bone defect regeneration with TNF/TNFR signaling involvement. *Adv Health Mater* **4**:1701–1708. <https://doi.org/10.1002/adhm.201500211>
- [8] Gharati G et al (2021) Comparison capacity of collagen hydrogel and collagen/strontium bioglass nanocomposite scaffolds with and without mesenchymal stem cells in regeneration of critical sized bone defect in a rabbit animal

- model. *Biol Trace Elem Res.* <https://doi.org/10.1007/s12011-021-02909-6>
- [9] Zhou XJ et al (2018) Mesoporous silica nanoparticles/gelatin porous composite scaffolds with localized and sustained release of vancomycin for treatment of infected bone defects. *J Mater Chem B* 6:740–752. <https://doi.org/10.1039/c7tb01246b>
- [10] Shim JH et al (2015) Comparative efficacies of a 3D-Printed PCL/PLGA/beta-TCP membrane and a titanium membrane for guided bone regeneration in beagle dogs. *Polymers-Basel* 7:2061–2077. <https://doi.org/10.3390/polym7101500>
- [11] Park SA, Lee SH, Kim WD (2011) Fabrication of porous polycaprolactone/hydroxyapatite (PCL/HA) blend scaffolds using a 3D plotting system for bone tissue engineering. *Bioproc Biosyst Eng* 34:505–513. <https://doi.org/10.1007/s00449-010-0499-2>
- [12] Zhou XQ et al (2021) Fabrication of polylactic acid (PLA)-based porous scaffold through the combination of traditional bio-fabrication and 3D printing technology for bone regeneration. *Colloid Surface B* 197:11420. <https://doi.org/10.1016/j.colsurfb.2020.111420>
- [13] Hu XY et al (2019) 3D Bio-printing of CS/Gel/HA/Gr hybrid osteochondral scaffolds. *Polymers-Basel* 11:1601. <https://doi.org/10.3390/polym11101601>
- [14] Fu, S. Y. *et al.* 3D printing of layered mesoporous bioactive glass/sodium alginate-sodium alginate scaffolds with controllable dual-drug release behaviors. *Biomed Mater* 14. <https://doi.org/10.1088/1748-605X/ab4166> (2019).
- [15] Zhai XY et al (2017) 3D-Printed high strength bioactive supramolecular polymer/clay nanocomposite hydrogel scaffold for bone regeneration. *Acs Biomater Sci Eng* 3:1109–1118. <https://doi.org/10.1021/acsbomaterials.7b00224>
- [16] Raafat AI, Kamal H, Sharada HM, Abd Elhalim SA, Mohamed RD (2020) Radiation synthesis of magnesium doped nano hydroxyapatite/(acacia-gelatin) scaffold for bone tissue regeneration: In Vitro Drug Release Study. *J Inorg Organomet P* 30:2890–2906. <https://doi.org/10.1007/s10904-019-01418-3>.
- [17] Viray CM, van Magill B, Zreiqat H, Ramaswamy Y (2022) Stereolithographic visible-light printing of poly(L-glutamic acid) hydrogel scaffolds. *Acs Biomater Sci Eng* 8:1115–1131. <https://doi.org/10.1021/acsbomaterials.1c01519>
- [18] Xu DL et al (2022) A composite deferoxamine/black phosphorus nanosheet/gelatin hydrogel scaffold for ischemic tibial bone repair. *Int J Nanomed* 17:1015–1030. <https://doi.org/10.2147/Ijn.S351814>
- [19] Rath SN et al (2012) Development of a pre-vascularized 3D scaffold-hydrogel composite graft using an arterio-venous loop for tissue engineering applications. *J Biomater Appl* 27:277–289. <https://doi.org/10.1177/0885328211402243>
- [20] Bendtsen ST, Quinnell SP, Wei M (2017) Development of a novel alginate-polyvinyl alcohol-hydroxyapatite hydrogel for 3D bioprinting bone tissue engineered scaffolds. *J Biomed Mater Res A* 105:1457–1468. <https://doi.org/10.1002/jbm.a.36036>
- [21] Bian, T. & Xing, H. A collagen(Col)/nano-hydroxyapatite (nHA) biological composite bone scaffold with double multi-level interface reinforcement. *Arabian Journal of Chemistry* 15. <https://doi.org/10.1016/j.arabjc.2022.103733> (2022).
- [22] Liu SH et al (2020) Designing vascular supportive albumen-rich composite bioink for organ 3D printing. *J Mech Behav Biomed* 104:103642. <https://doi.org/10.1016/j.jmbbm.2020.103642>
- [23] Liu SH et al (2022) Evaluation of different crosslinking methods in altering the properties of extrusion-printed chitosan-based multi-material hydrogel composites. *Bio-Des Manuf.* <https://doi.org/10.1007/s42242-022-00194-3>
- [24] Liu SH et al (2022) 3D printing of self-standing and vascular supportive multimaterial hydrogel structures for organ engineering. *Biotechnol Bioeng* 119:118–133. <https://doi.org/10.1002/bit.27954>
- [25] Hu Q et al (2021) Rapid fabrication of gelatin-based scaffolds with prevascularized channels for organ regeneration. *Biomed Mater* 16:045010. <https://doi.org/10.1088/1748-605X/abef7b>
- [26] Liu SH et al (2021) High-resolution combinatorial 3D printing of gelatin-based biomimetic triple-layered conduits for nerve tissue engineering. *Int J Biol Macromol* 166:1280–1291. <https://doi.org/10.1016/j.ijbiomac.2020.11.010>
- [27] Chuysinuan P et al (2021) Injectable eggshell-derived hydroxyapatite-incorporated fibroin-alginate composite hydrogel for bone tissue engineering. *Int J Biol Macromol* 193:799–808. <https://doi.org/10.1016/j.ijbiomac.2021.10.132>
- [28] Wu JW et al (2019) 3D printing mesoporous bioactive glass/sodium alginate/gelatin sustained release scaffolds for bone repair. *J Biomater Appl* 33:755–765. <https://doi.org/10.1177/0885328218810269>
- [29] Liang TT et al (2021) Drug-loading three-dimensional scaffolds based on hydroxyapatite-sodium alginate for bone regeneration. *J Biomed Mater Res A* 109:219–231. <https://doi.org/10.1002/jbm.a.37018>
- [30] Li Q et al (2019) Hydroxyapatite/collagen three-dimensional printed scaffolds and their osteogenic effects on human bone marrow-derived mesenchymal stem cells. *Tissue Eng Pt A* 25:1261–1271. <https://doi.org/10.1089/ten.tea.2018.0201>

- [31] Liu DK et al (2021) Synthesis and characterization of a hydroxyapatite-sodium alginate-chitosan scaffold for bone regeneration. *Front Mater* 8:648980. <https://doi.org/10.3389/fmats.2021.648980>
- [32] Bhat S, Uthappa UT, Altalhi T, Jung HY, Kurkuri MD (2022) Functionalized porous hydroxyapatite scaffolds for tissue engineering applications: a focused review. *ACS Biomater Sci Eng* 8:4039–4076. <https://doi.org/10.1021/acsbiomaterials.1c00438>
- [33] Cicuendez M et al (2018) Multifunctional pH sensitive 3D scaffolds for treatment and prevention of bone infection. *Acta Biomater* 65:450–461. <https://doi.org/10.1016/j.actbio.2017.11.009>
- [34] Mulazzi M et al (2021) Medicated hydroxyapatite/collagen hybrid scaffolds for bone regeneration and local antimicrobial therapy to prevent bone infections. *Pharmaceutics* 13:1090. <https://doi.org/10.3390/pharmaceutics13071090>
- [35] Loca D, Sokolova M, Locs J, Smirnova A, Irbe Z (2015) Calcium phosphate bone cements for local vancomycin delivery. *Mat Sci Eng C-Mater* 49:106–113. <https://doi.org/10.1016/j.msec.2014.12.075>
- [36] Rajabi A, Esmaeili A (2020) Preparation of three-phase nanocomposite antimicrobial scaffold BCP/Gelatin/45S5 glass with drug vancomycin and BMP-2 loading for bone regeneration. *Colloid Surface A* 606:125508. <https://doi.org/10.1016/j.colsurfa.2020.125508>
- [37] Jiang XD et al (2021) A combined experimental and molecular dynamics simulation study on doxorubicin adsorption on strontium-substituted hydroxyapatite hollow microspheres. *Appl Surf Sci* 542:148667. <https://doi.org/10.1016/j.apsusc.2020.148667>
- [38] Qiao SC et al (2020) The combination of multi-functional ingredients-loaded hydrogels and three-dimensional printed porous titanium alloys for infective bone defect treatment. *J Tissue Eng* 11. <https://doi.org/10.1177/2041731420965797>
- [39] Prasanna APS, Venkatasubbu GD (2018) Sustained release of amoxicillin from hydroxyapatite nanocomposite for bone infections. *Prog Biomater* 7:289–296. <https://doi.org/10.1007/s40204-018-0103-4>
- [40] Bakhsheshi-Rad HR, Hamzah E, Abbasizadeh N, Najafinezhad A, Kashefian M (2018) Synthesis of novel nanostructured bredigite-amoxicillin scaffolds for bone defect treatment: cytocompatibility and antibacterial activity. *J Sol-Gel Sci Techn* 86:83–93. <https://doi.org/10.1007/s10971-018-4606-1>
- [41] Krishnan AG, Biswas R, Menon D, Nair MB (2020) Biodegradable nanocomposite fibrous scaffold mediated local delivery of vancomycin for the treatment of MRSA infected experimental osteomyelitis. *Biomater Sci-Uk* 8:2653–2665. <https://doi.org/10.1039/d0bm00140f>
- [42] Uthappa UT, Bhat MP, Jung H-Y, Kurkuri MD (2021) In: Devarajan Thangadurai, Jeyabalan Sangeetha, Ram Prasad (eds) *Bioprospecting algae for nanosized materials*. Springer International Publishing, Cham, pp 275–289.
- [43] Kolanthai E, Ganesan K, Epple M, Kalkura SN (2016) Synthesis of nanosized hydroxyapatite/agarose powders for bone filler and drug delivery application. *Mater Today Commun* 8:31–40. <https://doi.org/10.1016/j.mtcomm.2016.03.008>
- [44] Ferraz, M. P., Mateus, A. Y., Sousa, J. C. & Monteiro, F. J. Nanohydroxyapatite microspheres as delivery system for antibiotics: Release kinetics, antimicrobial activity, and interaction with osteoblasts. *J Biomed Mater Res A* 81a, 994–1004. <https://doi.org/10.1002/jbm.a.31151> (2007).
- [45] Zhao Q et al (2019) Adsorption behavior of drugs on hydroxyapatite with different morphologies: a combined experimental and molecular dynamics simulation study. *Ceram Int* 45:19522–19527. <https://doi.org/10.1016/j.ceramint.2019.06.068>
- [46] Liu SF et al (2020) Sodium alginate/collagen composite multiscale porous scaffolds containing poly(epsilon-caprolactone) microspheres fabricated based on additive manufacturing technology. *Rsc Adv* 10:39241–39250. <https://doi.org/10.1039/d0ra04581k>
- [47] Sun X, Tong S, Yang SD, Guo S (2021) The effects of graphene on the biocompatibility of a 3D-printed porous titanium alloy. *Coatings* 11:1509. <https://doi.org/10.3390/coatings11121509>
- [48] Iglesias-Mejuto A, Garcia-Gonzalez CA (2022) 3D-Printed, dual crosslinked and sterile aerogel scaffolds for bone tissue engineering. *Polymers-Basel* 14:1211. <https://doi.org/10.3390/polym14061211>
- [49] Kolanthai E et al (2015) Effect of solvent; enhancing the wettability and engineering the porous structure of a calcium phosphate/agarose composite for drug delivery. *Rsc Adv* 5:18301–18311. <https://doi.org/10.1039/c4ra14584d>
- [50] Iqbal DN et al (2021) Enhanced antibacterial activity of chitosan, guar gum and polyvinyl alcohol blend matrix loaded with amoxicillin and doxycycline hyclate drugs. *Arab J Chem* 14. <https://doi.org/10.1016/j.arabjc.2021.103156> (2021).
- [51] Ajallouei F et al (2022) Amoxicillin-loaded multilayer pullulan-based nanofibers maintain long-term antibacterial properties with tunable release profile for topical skin delivery applications. *Int J Biol Macromol* 215:413–423. <https://doi.org/10.1016/j.ijbiomac.2022.06.054>
- [52] Pupo YM et al (2021) Effect of Hydroxyapatite microspheres, amoxicillin-hydroxyapatite and collagen-

- hydroxyapatite composites on human dental pulp-derived mesenchymal stem cells. *Materials* 14:7515. <https://doi.org/10.3390/ma14247515>
- [53] Wu MH et al (2020) Biomimetic mineralization of novel hydroxyethyl cellulose/soy protein isolate scaffolds promote bone regeneration in vitro and in vivo. *Int J Biol Macromol* 162:1627–1641. <https://doi.org/10.1016/j.ijbiomac.2020.08.029>
- [54] Farzamfar S et al (2019) Tetracycline hydrochloride-containing poly (epsilon-caprolactone)/poly lactic acid scaffold for bone tissue engineering application: in vitro and in vivo study. *Int J Polym Mater Po* 68:472–479. <https://doi.org/10.1080/00914037.2018.1466133>
- [55] Hu D, Ren Q, Li ZC, Zhang LL (2020) Chitosan-based biomimetically mineralized composite materials in human hard tissue repair. *Molecules* 25:4785. <https://doi.org/10.3390/molecules25204785>
- [56] Li XZ et al (2020) Osteoblastic differentiation of stem cells induced by graphene oxide-hydroxyapatite-alginate hydrogel composites and construction of tissue-engineered bone. *J Mater Sci-Mater M* 31:125. <https://doi.org/10.1007/s10856-020-06467-6>
- [57] Turco G et al (2009) Alginate/hydroxyapatite biocomposite for bone ingrowth: a trabecular structure with high and isotropic connectivity. *Biomacromol* 10:1575–1583. <https://doi.org/10.1021/bm900154b>
- [58] Liu SF et al (2019) Bioactive and biocompatible macroporous scaffolds with tunable performances prepared based on 3D printing of the pre-crosslinked sodium alginate/hydroxyapatite hydrogel ink. *Macromol Mater Eng* 304:1800698. <https://doi.org/10.1002/mame.201800698>
- [59] Xing F et al (2021) Chitin-hydroxyapatite-collagen composite scaffolds for bone regeneration. *Int J Biol Macromol* 184:170–180. <https://doi.org/10.1016/j.ijbiomac.2021.05.019>
- [60] Gilarska A, Lewandowska-Lancucka J, Horak W, Nowakowska M (2018) Collagen/chitosan/hyaluronic acid—based injectable hydrogels for tissue engineering applications—design, physicochemical and biological characterization. *Colloid Surface B* 170:152–162. <https://doi.org/10.1016/j.colsurfb.2018.06.004>
- [61] Pandithevan P, Kumar GS (2010) Finite element analysis of a personalized femoral scaffold with designed microarchitecture. *P I Mech Eng H* 224:877–889. <https://doi.org/10.1243/09544119jeim633>
- [62] Cheng MQ et al (2016) A novel open-porous magnesium scaffold with controllable microstructures and properties for bone regeneration. *Sci Rep* 6:24134. <https://doi.org/10.1038/srep24134>
- [63] Guo R et al (2022) Mechanical stability and biological activity of Mg-Sr co-doped bioactive glass/chitosan composite scaffolds. *J Non-Cryst Solids* 583:121481. <https://doi.org/10.1016/j.jnoncrysol.2022.121481>
- [64] Wei Z, Wu C, Li R, Yu D, Ding Q (2021) Nanocellulose based hydrogel or aerogel scaffolds for tissue engineering. *Cellulose* 28:7497–7520. <https://doi.org/10.1007/s10570-021-04021-3>
- [65] Furtos G, Rivero G, Rapuntean S, Abraham GA (2017) Amoxicillin-loaded electrospun nanocomposite membranes for dental applications. *J Biomed Mater Res B* 105:966–976. <https://doi.org/10.1002/jbm.b.33629>

Publisher's Note Springer Nature remains neutral with regard to jurisdictional claims in published maps and institutional affiliations.

Springer Nature or its licensor (e.g. a society or other partner) holds exclusive rights to this article under a publishing agreement with the author(s) or other rightsholder(s); author self-archiving of the accepted manuscript version of this article is solely governed by the terms of such publishing agreement and applicable law.